

# Vibration and Noise Optimization of New Asymmetric Modular PMaSynRM

Guohai Liu, Akang Gao, Qian Chen\*, Yanxin Mao and Gaohong Xu

(School of Electrical and Information Engineering, Jiangsu University, Zhenjiang 212013, China)

**Abstract:** An optimized structure to weaken the vibration and noise of a new asymmetric permanent magnet-assisted synchronous reluctance motor (PMaSynRM) is proposed. The new asymmetric PMaSynRM has the advantages of a low torque ripple and high fault tolerance. However, the asymmetric structure generates an unbalanced magnetic force (UMF), which results in vibration and noise problems. In this study, the vibration and noise of the motor are analyzed and optimized. First, the radial pressure is analyzed, and an optimized structure is proposed. The electromagnetic performance of the motor before and after optimization is analyzed using the finite element method. Second, a three-dimensional model is established, and modal analysis is conducted considering the orthotropy of the stator and effective windings. Finally, the vibration and noise are simulated and analyzed, and the validity of the analysis results is verified experimentally. The analysis results indicate that the optimized motor realizes a reduction in the motor vibration and noise.

**Keywords:** Modular motor, asymmetric structure, modal analysis, vibration and noise analysis, unbalanced magnetic force

## 1 Introduction

The development of the permanent magnet (PM) motor is restricted by the high price of the NdFeB, to reduce production costs, researchers have proposed the permanent magnet assisted synchronous reluctance motor (PMaSynRM) [1]. This motor has the advantages of an acceptable torque density and high efficiency, and only requires inexpensive ferrite. In recent years, more attention has been paid to the optimization of the structure to improve the electromagnetic performance [2-3]. Asymmetric stators and rotors have been proposed to suppress torque ripple [4]; however, the asymmetric structure generates an unbalanced magnetic force (UMF), creating new problems of vibration and noise. Asymmetric structures have serious vibration problems at high speeds [5]. However, their mechanisms have not been thoroughly studied and the sources of the vibration and noise have not been clearly explained. In some studies, the sources of the vibration and noise in symmetric PMaSynRM

were analyzed. The slot harmonic and its multiples are the main reasons for vibration [6]; however, the influence of the windings is not considered in the modal analysis. For the integer-slot symmetric PMaSynRM, the vibration of the motor is mainly caused by the zero-order radial force. However, the vibration of an asymmetric motor is different from that of a symmetric motor. The UMF generated by the asymmetric motor causes the vibration to change significantly. Previous studies on UMF have primarily focused on rotor eccentricity or asymmetric windings [7-9]. The influence of the UMF generated by the asymmetric structure on the vibration has not received much attention. There is no effective method for optimizing the vibration and noise of asymmetric motors. Therefore, it is important to optimize the vibration of an asymmetric motor.

For small- and medium-sized motors, if the machining accuracy is sufficiently high and the aerodynamic noise is small, electromagnetic noise is the focus [10]. Research on electromagnetic vibration is mainly from two aspects: radial force, which plays a major role, and tangential force, which plays a minor role. For electromagnetic force analysis, the finite element (FE) and analytical methods are mainly used [11-12]. In the analytical method, saturation is omitted, causing low accuracy. The FE method yielded

Manuscript received January 11, 2022; revised April 5, 2022; accepted May 5, 2022. Date of publication June 30, 2023; date of current version October 22, 2022.

\* Corresponding Author, E-mail: chenqian0501@ujs.edu.cn

Digital Object Identifier: 10.23919/CJEE.2023.000006

accurate results but could not clearly reflect the influence of the motor parameters on the electromagnetic force. Therefore, this study combines the two methods and evolves into a semi-analytical method [13-14]. Resonance occurs when the frequency of the electromagnetic force is close to the natural frequency of the structural mode with the same spatial order. Heavy resonance damages the motor parts and affects normal motor use. Therefore, a modal analysis is necessary. In some existing studies, the orthotropy of the stator lamination was not considered and the windings were generally regarded as the additional mass of the stator. In recent years, studies have deduced that an efficient equivalent model of the stator and winding has a significant influence on the accuracy of modal analysis [15-17]. Vibration and noise studies have mainly focused on source analysis and weakening. The radial force that causes high vibrations can be reduced by optimizing the motor structure [18-22]. Additionally, an appropriate control strategy can be used to reduce noise [23].

In this study, the vibration and noise of an asymmetric PMaSynRM were analyzed. Based on the analysis results, an optimized structure was proposed to reduce vibration and noise. In Section 2, the topology of an asymmetric PMaSynRM is presented. In Section 3, the radial pressure is analyzed and an optimized structure is proposed through the analysis of the rotor permeance. The electromagnetic performance of the motor before and after optimization was analyzed using the FE method. The modal analysis is presented in Section 4, particularly considering the effects of the stator laminations and effective windings. In Section 5, combined with the radial pressure and structural modal analysis, the vibration and noise of the PMaSynRM are analyzed in detail. In Section 6, the prototype is manufactured to verify the validity of the analysis results. Finally, the conclusions are presented in Section 7.

## 2 Topology machines

To solve the problem of a large torque ripple in general PMaSynRMs and improve the fault tolerance of the motor, a new asymmetric modular structure is

proposed [4]. The cross-section of the PMaSynRM is shown in Fig. 1. Tab.1 lists the main parameters of the motor. The cross-section of the rotor is shown in Fig. 2. Tab. 2 lists the main rotor parameters.

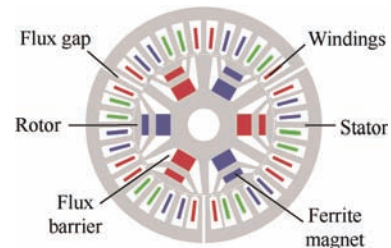
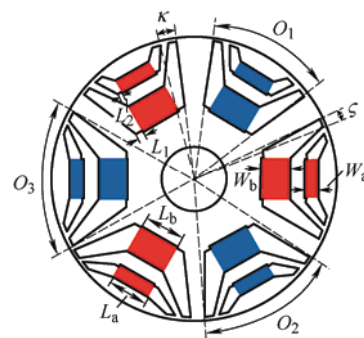


Fig. 1 Asymmetric PMaSynRM

Tab. 1 Main parameters of the PMaSynRM

Parameter	Value
Number of slots	36
Number of poles	6
PM	Ferrite
Lamination	DW470_50
Stator outer diameter/mm	150
Stator inner diameter/mm	90
Axial stack length/mm	100
Air-gap thickness/mm	0.5
Rotor outer diameter/mm	89
Rotor inner diameter/mm	20
Width of flux gap/mm	2
Current/A	10
Rated speed/(r/min)	1 600
Rated torque/(N · m)	9.7



The asymmetric stator is evenly divided into three modules by the flux gap, each of which is composed of a set of independent three-phase distributed windings. This helps improve the fault tolerance of the motor. The source of the main torque harmonics of the PMSynRM changed after a flux gap was added. Therefore, the stator slots on both sides of the flux gap are shifted at different angles, whereas the positions of the other slots in the module remain unchanged. A multiparameter optimization method was used to obtain the appropriate offset angle. Finally, an appropriate asymmetric structure was constructed. The asymmetrical design causes a phase shift of the torque waveform, thus, the mutual compensation of the torque can be realized. This helps reduce the torque ripple. The teeth widths decreased owing to the insertion of the flux gap at the end of each module. In this motor, different flux barrier angles reduce the torque ripple. Compared with the symmetric structure, the torque ripple of the asymmetric structure was reduced by approximately 28%. However, an asymmetric structure leads to rich radial force harmonics, including the first-order radial force. The UMF intensified the motor vibrations. Therefore, it is essential to analyze and optimize the vibrations of the asymmetric motor.

### 3 Electromagnetic analysis

#### 3.1 Radial pressure analysis

The radial force acting on the stator surface is the main cause of the motor vibration. The tangential force acting on the stator teeth causes the local deformation and vibration of the motor. However, the amplitude of the tangential force is negligible compared to that of the radial force; therefore, the influence of the tangential force can be ignored in this work.

According to the Maxwell Stress Tensor method<sup>[10]</sup>, the radial pressure  $P_r$  and tangential pressure  $P_t$  can be expressed as

$$P_r = \frac{1}{2\mu_0} (B_r^2 - B_t^2) \approx \frac{B_r^2}{2\mu_0} \quad (1)$$

$$P_t = \frac{1}{\mu_0} B_r B_t \quad (2)$$

where  $B_r$  and  $B_t$  are the radial and tangential

components, respectively, of the air-gap flux density. Because the tangential component of the air-gap flux density is much smaller than the radial component, it can be ignored. Therefore, the radial pressure can be approximated as the square of the radial flux density.

Ignoring the current harmonics, the stator magnetomotive force can be expressed as

$$f_s(\theta, t) = \begin{cases} \sum_v F_v \cos(\omega t - vp\theta) & v = 6k - 5 \\ \sum_v F_v \cos(\omega t + vp\theta) & v = 6k - 1 \end{cases} \quad (3)$$

where  $\theta$  is the spatial position of the rotor,  $t$  is time,  $\omega$  is the mechanical angular speed,  $p$  is the number of pole pairs,  $F_v$  is the amplitude of the  $v$ -order stator magnetomotive force, and  $k$  is a positive integer.

The rotor magnetomotive force can be expressed as

$$f_r(\theta, t) = \sum_\mu F_\mu \cos(\mu\omega t - \mu p\theta) \quad \mu = 2i + 1 \quad (4)$$

where  $F_\mu$  is the amplitude of the  $\mu$ -order rotor magnetomotive force and  $i$  is the natural number.

Owing to the asymmetric slotting of the stator and the influence of the flux gap, the permeance of the stator is divided into three periods along the circumferential direction; that is, its spatial period number is three. Fig. 3 shows the equivalent permeance diagram of the asymmetric stator during one period.

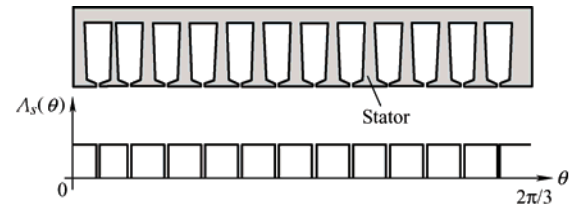


Fig. 3 Equivalent diagram of stator permeance for one period

The relative permeance of the asymmetric stator can be expanded using a Fourier series and can be expressed as

$$A_s(\theta, t) = A_{s0} + \sum_m A_{sm} \cos\left(\frac{mz\theta}{12}\right) \quad (5)$$

where  $A_{s0}$  and  $A_{sm}$  are the average and  $m$ -order permeance harmonic amplitudes of the stator permeance, respectively;  $z$  is the slot number; and  $m$  is a positive integer.

Fig. 4 shows the equivalent permeance of the rotor. Owing to the asymmetry of the flux barrier, the spatial period number was 1.

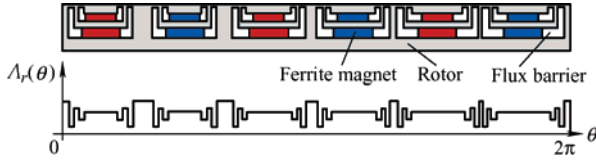


Fig. 4 Equivalent diagram of rotor permeance

The relative permeance of the asymmetric rotor can be expressed as

$$A_r(\theta, t) = A_{r0} + \sum_n A_{rn} \cos\left(\frac{ncot}{3} - \frac{np\theta}{3}\right) \quad (6)$$

where  $A_{r0}$  and  $A_{rn}$  are the average and  $n$ -order permeance harmonic amplitudes of the rotor permeance, respectively, and  $n$  is a positive integer.

Air-gap relative permeance can be expressed as

$$A(\theta, t) = A_s(\theta, t) \cdot A_r(\theta, t) \quad (7)$$

The radial pressure is denoted by

$$P_r \approx \frac{1}{2\mu_0} \left\{ [f_s(\theta, t) + f_r(\theta, t)] \times A(\theta, t) \right\}^2 \quad (8)$$

The order and frequency of the radial pressure can be obtained using Eq. (8). Tab. 3 lists the partial result of the radial pressure obtained by the decomposition of the asymmetric motor. It can be observed that the radial pressure harmonics of the asymmetric motor are very rich. The first-order radial pressure, that is, the UMF, is mainly caused by the asymmetric rotor and stator. From the analytical analysis, it is clear that the source harmonics of the radial pressures can be obtained, which contributes to future optimization.

Tab. 3 Radial pressure of asymmetric motor

Amplitude	Frequency	Order	Source
$\frac{A_{s0}^2 A_{r0}^2 F_v^2}{4\mu_0}$	$2pf_r$	$6v$	Armature
$\frac{A_{s0}^2 F_{v1} F_{v2} A_{n1} A_{n2}}{16\mu_0}$	$\left(\frac{n_1}{3} \pm \frac{n_2}{3}\right) pf_r$	$3(v_1 \pm v_2) \pm (n_1 \pm n_2)$	
$\frac{A_{s0} F_{v1} F_{v2} A_{n1} A_{n2} A_m}{32\mu_0}$	$\left(2 \pm \frac{n_1}{3} \pm \frac{n_2}{3}\right) pf_r$	$3(v_1 \pm v_2 \pm m) \pm (n_1 \pm n_2)$	
$\frac{A_{s0}^2 A_{r0}^2 F_\mu^2}{4\mu_0}$	$2\mu pf_r$	$6\mu$	PM
$\frac{A_{s0}^2 F_{\mu1} F_{\mu2} A_{n1} A_{n2}}{8\mu_0}$	$\left(\mu_1 \pm \mu_2 \pm \frac{n_1}{3} \pm \frac{n_2}{3}\right) pf_r$	$3(\mu_1 \pm \mu_2) \pm (n_1 \pm n_2)$	
$\frac{A_{r0} F_{\mu1} F_{\mu2} A_{n1} A_{n2} A_n}{16\mu_0}$	$\left(\mu_1 \pm \mu_2 \pm \frac{n}{3}\right) pf_r$	$3(\mu_1 \pm \mu_2) \pm 3(m_1 \pm m_2) \pm n$	
$\frac{A_{s0}^2 A_{r0}^2 F_v F_\mu}{4\mu_0}$	$(1 \pm \mu) pf_r$	$3(v \pm \mu)$	Armature and PM
$\frac{A_{s0}^2 F_v F_\mu A_{n1} A_{n2}}{16\mu_0}$	$\left(1 \pm \mu \pm \frac{n_1}{3} \pm \frac{n_2}{3}\right) pf_r$	$3(v \pm \mu) \pm (n_1 \pm n_2)$	
$\frac{A_{r0} F_v F_\mu A_{n1} A_{n2} A_n}{32\mu_0}$	$\left(1 \pm \mu \pm \frac{n}{3}\right) pf_r$	$3\left(v \pm \mu \pm \frac{n}{3}\right) \pm n$	

According to the results of the radial pressure analysis, the first-order radial pressure was closely related to the rotor permeance. The asymmetric rotor causes the rotor permeance harmonics to have other orders except the  $6i$ -order, where  $i$  is the natural number, and some harmonics are the main source of the UMF. The UMF was reduced by reducing the amplitude of these harmonics. Therefore, the rotor can be optimized to reduce the relevant rotor permeance harmonics and suppress the vibration and noise caused by the UMF.

### 3.2 Vibration and noise optimization process

For asymmetric motors, the UMF should receive more attention. According to the above analysis, reducing the relevant rotor permeance harmonics will reduce the UMF; therefore, the rotor is the focus of optimization in this work.

The relative permeance of the rotor was obtained as shown in Fig. 5. Motor structures with a slotted and solid rotors are established. The permanent magnets were placed in the circumferential direction and magnetized in the radial direction. The flux densities of the two structures were obtained using the FE method. After the FE simulation, the observation path circle in the air gap was selected to obtain the air-gap flux density. The ratio of the two flux densities was the rotor relative permeance, which reflects the effect of the rotor slotting on the flux density.

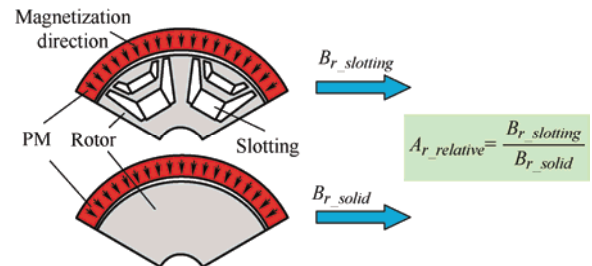


Fig. 5 Process of obtaining rotor relative permeance

Fig. 6 shows the symmetric and asymmetric rotors. The main difference between the symmetric and asymmetric structures lies in the different opening angles of the flux barrier. The permeance of the two structures are analyzed. Fig. 7 shows the symmetric and asymmetric rotor permeance harmonics. The order of the rotor permeance harmonics of the symmetric rotor is  $6i$ , where  $i$  is a natural number. The zero-order rotor relative permeance is the invariant part of the rotor relative permeance. The main wave of the flux

density is generated by the fundamental wave of the magnetomotive force and the zero-order air-gap permeance. However, there are harmonics of the non- $6i$  order in the asymmetric rotor. Some of these harmonics are the main sources of the UMF and the key to optimization.

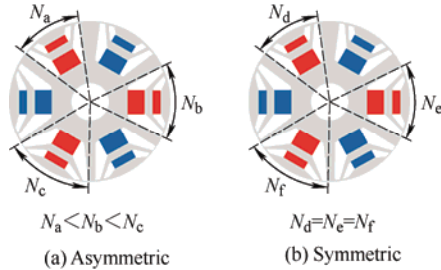


Fig. 6 Rotor of PMaSynRMs

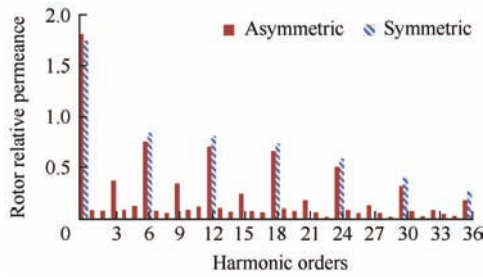


Fig. 7 Rotor relative permeance harmonic

Fig. 8 shows the process of vibration and noise optimization in this work. The optimization of the asymmetric motor mainly focuses on finding the source. Considering the asymmetric structure, the

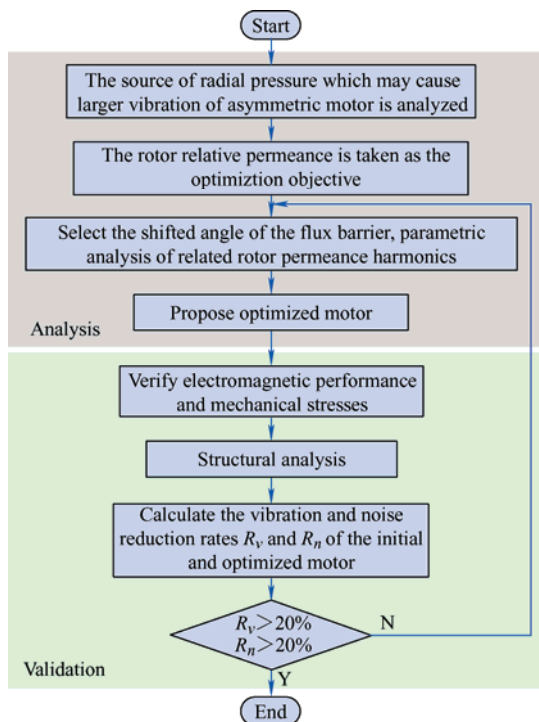


Fig. 8 Flow chart of vibration and noise optimization of the asymmetric motor

radial force harmonics are very rich. To facilitate the analysis, the relationship between the radial force and structure is established based on the rotor relative permeance, and the permeance is taken as the optimization objective.

### 3.3 Proposed optimization structure

The topology of the asymmetric PMaSynRM rotor is illustrated in Fig. 9. Different angles of  $\beta$  and  $\sigma$  affect the distribution of the rotor permeance. The  $\beta$  and  $\sigma$  of the initial motor are  $51.56^\circ$  and  $6.33^\circ$ , respectively. The two adjacent magnetic poles are a pair of poles. The structure of the pair of pole flux barriers was similar.

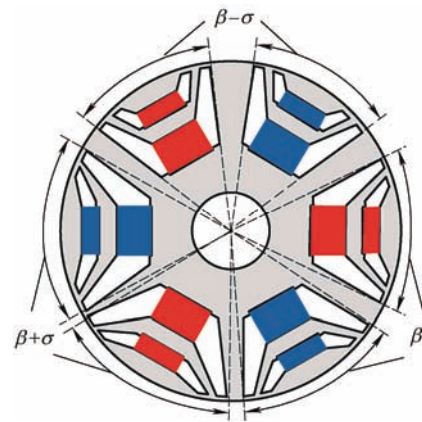


Fig. 9 Asymmetric PMaSynRM rotor

The amplitude of the radial force density was less affected by ferrite, and its influence could be ignored in the simplified analysis. The order and frequency of the flux density generated by the stator magnetomotive force and permeance are listed in Tab. 4. If the radial force density  $(-1, f_r)$  is generated, the flux density harmonics interaction with different frequencies is required, and the frequency generated is  $3f_r \pm (1 \pm n/3)3f_r$ , where  $n$  is 1 or 5. Therefore, the source of the UMF is mainly affected by the first- and fifth-order rotor permeance harmonics.

Tab. 4 Order and frequency of flux density produced by stator magnetomotive force

Stator magnetomotive force and permeance	Frequency	Order
Stator magnetomotive force and average permeance	$3f_r$	$3v$
Stator magnetomotive force and rotor permeance harmonics	$(1 \pm n/3)3f_r$	$3v \pm n$
Stator magnetomotive force and stator permeance harmonics	$3f_r$	$3v \pm 3m$
Stator magnetomotive force and common permeance harmonics	$(1 \pm n/3)3f_r$	$3v \pm 3m \pm n$



To select the appropriate flux barrier opening angle, parametric optimization of the motor was performed using two variables [24]. The basic principles for selecting variables  $\sigma$  and  $\beta$  are  $\sigma_1(1\pm 15\%)$  and  $\beta_1(1\pm 15\%)$ , where  $\sigma_1$  and  $\beta_1$  are the initial values. When these two parameters are too large, there may be a deformation of the flux barrier shape and an overlap between the flux barriers. These effects were considered in this study. Finally, the range of  $\sigma$  was  $1^\circ$  to  $7^\circ$ , whereas the range of  $\beta$  was  $48^\circ$  to  $58^\circ$ . The torque ripple and first- and fifth-order rotor permeances between  $\beta$  and  $\sigma$  are shown in Figs. 10 and 11, respectively. It can be noted that there is a conflicting relationship between the rotor permeance and torque ripple. A function that adds these three values and then takes a relatively small sum is constructed. The constructed function is as follows

$$G_{\min}(x) = \lambda_1 \frac{T_{rip}(x)}{T_{rip_0}} + \lambda_2 \frac{A_{r1}(x)}{A_{r1_0}} + \lambda_3 \frac{A_{r5}(x)}{A_{r5_0}} \quad (9)$$

where  $G_{\min}(x)$  is the objective function of the overall optimization, which aims to determine the minimum value in the optimization process.  $\lambda_1$ ,  $\lambda_2$ , and  $\lambda_3$  are the weights of the torque ripple, first-order, and fifth-order rotor relative permeance, respectively.  $\lambda_1$ ,  $\lambda_2$ , and  $\lambda_3$  were set as 0.4, 0.3, and 0.3, respectively. The purpose of assigning large torque-ripple weights is to ensure that the torque performance is not compromised as much as possible.  $T_{rip_0}$ ,  $A_{r1_0}$ , and  $A_{r5_0}$  are the initial values of the torque ripple, first-order, and fifth-order rotor relative permeance, respectively.  $T_{rip}(x)$ ,  $A_{r1}(x)$ , and  $A_{r5}(x)$  are the values of the torque ripple, first-order, and fifth-order rotor relative permeance transformed with the selected variables, respectively.

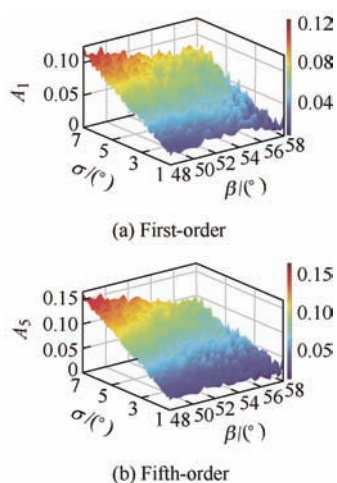


Fig. 10 Rotor permeance distribution between  $\beta$  and  $\sigma$

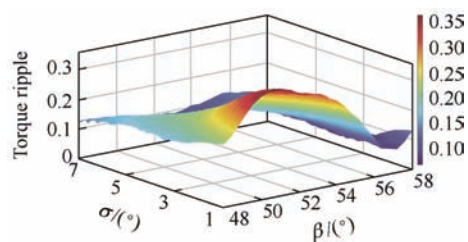


Fig. 11 Torque ripple distribution between  $\beta$  and  $\sigma$

The value of  $G_{\min}(x)$  was calculated based on the parameterized scanning results. Fig. 12 shows the scatter points of the comparison of the objective optimization function results of the different optimization models. According to the analysis, the smaller the value of  $G_{\min}(x)$ , the better the performance of the vibration and noise. As shown in Fig. 12, when  $G_{\min}(x)$  takes the minimum value, that is, the optimized model position,  $\sigma$  is  $3^\circ$  and  $\beta$  is  $55.6^\circ$ . Fig. 13 shows the optimized rotor.

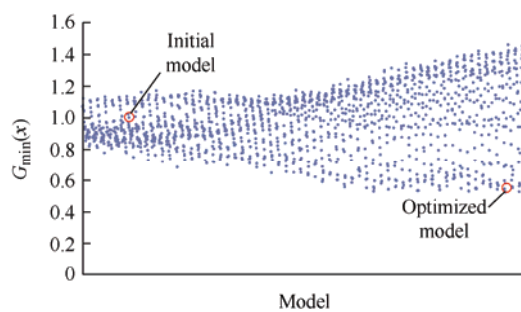


Fig. 12  $G_{\min}(x)$  comparison of different optimization models

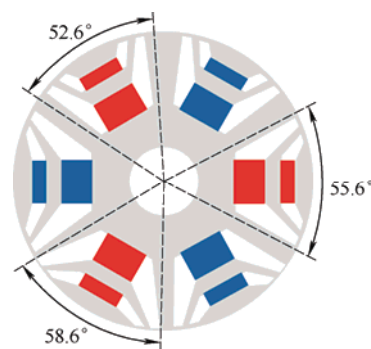


Fig. 13 Optimized rotor

Compared with the initial rotor, the optimized rotor has thinner magnetic ribs; therefore, stress checking is required to verify whether the optimized rotor meets the stress intensity of the core material. The computed stress distribution at 1 600 r/min is shown in Fig. 14. It can be observed that the maximum stress of the optimized rotor is 3.23 MPa, which is less than the ultimate stress of silicon steel material. Therefore, the

optimized rotor satisfies the stress requirements.

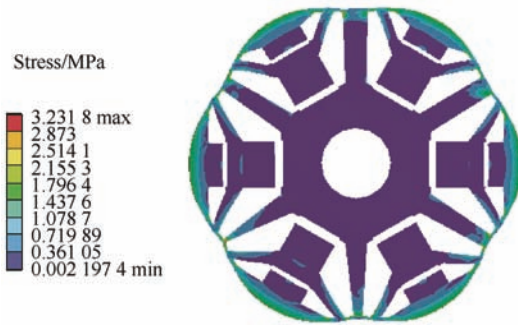


Fig. 14 Mechanical stress nephogram

### 3.4 FE analysis

Finite element simulation models of the initial and optimized motor were established, and the electromagnetic performance was simulated and analyzed. The stator structure and winding arrangement of the two models were the same. The excitation conditions of the two models were identical. The difference was in the rotor structures. The opening angles of the flux barriers of the two models were different. The initial results were the simulation results for the rotor of the original model, and the optimized results were the simulation results of the optimized rotor. The output torque is shown in Fig. 15. The average torque values of the initial and optimized motor are  $9.74 \text{ N} \cdot \text{m}$  and  $9.54 \text{ N} \cdot \text{m}$ , respectively, and the torque ripple is 16.1% and 18.9% respectively. Because the main amplitude of the flux density of the motor was reduced after optimization, the average torque was slightly reduced. The torque of the optimized motor was not sacrificed.

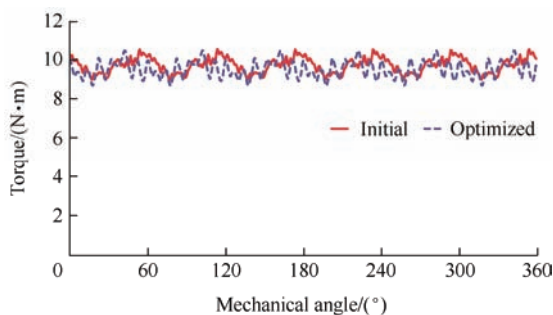


Fig. 15 Torque comparison of two motors

In this study, the motor structure differed before and after optimization. This resulted in a difference in the air-gap permeance. Therefore, it is necessary to

analyze the air-gap permeance. The relative permeance of the air gap can be obtained indirectly by analyzing the flux densities of different motor models.

Through an analysis of the radial pressure, it was deduced that the asymmetry of the rotor is the main reason for the UMF. Therefore, the focus is on the analysis of the rotor permeance. Fig. 16 shows the relative permeance of the rotor and its harmonics. As demonstrated in the rotor permeance harmonics in Fig. 16b, compared with the initial motor, the harmonic amplitudes of the first-order and fifth-order rotor permeances of the optimized motor are reduced by 59.9% and 65%, respectively. The interaction between the permeance and magnetomotive force generates the flux density. Radial pressure is generated by the interaction of different flux densities. Therefore, the UMF of the optimized motor was reduced.

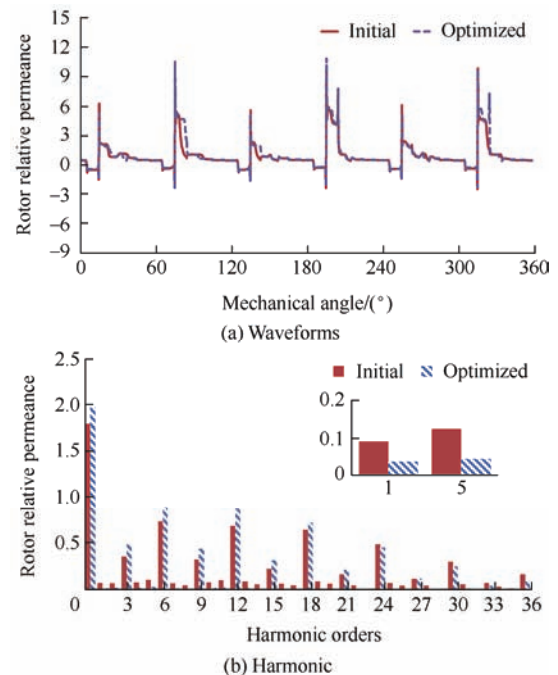


Fig. 16 Rotor relative permeance

The flux density under load is simulated and analyzed. Fig. 17 shows the radial flux density and Fourier decomposition of the two motors, respectively. The orders of the flux density harmonics of the two motors are mainly  $3\mu$ . However, except for these harmonics, there are other flux density harmonics in the asymmetric motors that generate UMF. These non- $3\mu$ -order harmonics in the optimized motor are

small, which weakens the UMF.

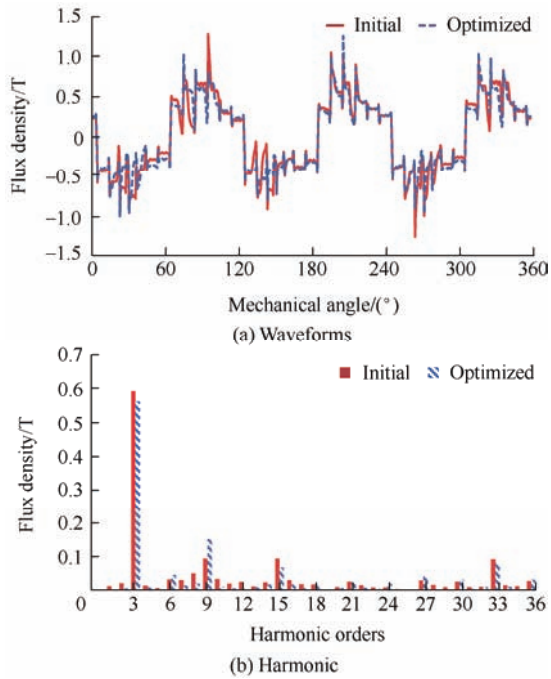


Fig. 17 Air-gap flux density

The radial pressure is a function of space and time, hence, it needs to be analyzed in two dimensions. Fig. 18a shows the two-dimensional Fourier decomposition of the radial pressure in the initial motor. The radial pressure distribution is consistent with the theoretical analysis. Low-order radial pressures are more likely to cause larger vibration and noise. However, the spatial order of the radial pressure on the stator teeth is not necessarily equal to its spatial order in the air-gap. Owing to the action of the stator teeth, some high-order radial pressures can be equivalent to low-order radial pressures after transformation. Therefore, some high-order radial forces may also cause lower-order vibration [25]. Therefore, the first-order and 37th-order radial pressure harmonics generated by the asymmetric structure can both cause first-order vibration, hence the first- and 37th-order harmonics should be focused on. Fig. 18b shows the two-dimensional Fourier decomposition of the radial pressure in the optimized motor. The first-order radial pressure is reduced from  $0.456 \text{ N/cm}^2$  to  $0.246 \text{ N/cm}^2$ , which decreases by 46.1%. Therefore, the optimized motor can suppress the large vibration caused by the UMF.

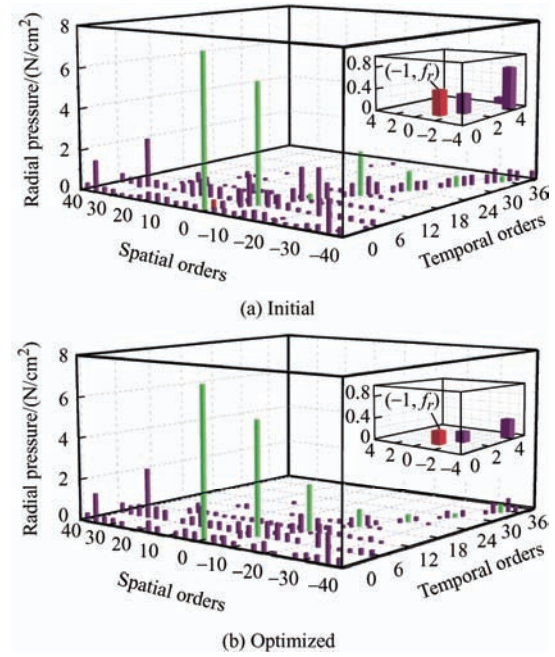


Fig. 18 Radial pressure harmonics

#### 4 Structural analysis

The resonance affects normal operation and shortens the service life of the motor. Therefore, the main purpose of the modal analysis is to avoid resonance. The FE method has gradually become the mainstream analysis method, owing to its more accurate results. In this study, the FE method and experiment were combined to complete the modal analysis.

Fig. 19 shows a three-dimensional model of the initial prototype. In this study, the effective winding is equivalent to a cylinder of an approximate shape. The winding density was estimated based on the proportion of the copper wire, insulation, and air in the slot. The simulation of the entire machine is time-consuming, and there are many variables. However, this is difficult to achieve. Thus, the simplified model does not consider the rotor and shaft, which have a slight effect on the natural frequency. The stiffness and mass effects of the end winding can be offset; therefore, the end winding can be ignored. According to the experimental results, the modal parameters of the stator and winding were adjusted such that the simulation results were close to the experimental results. The natural frequencies of the two motors are very close, owing to the small difference in their structures.



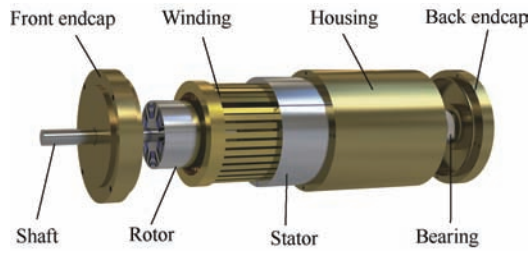


Fig. 19 Three-dimensional model of the prototype

Owing to the rich radial force harmonics of an asymmetric motor, resonance is almost inevitable. An accurate modal analysis is particularly important for accurately reflecting the vibration of the motor.

Fig. 20 shows the test diagram of the modal experiment. The modal test of the motor under free conditions was completed using the hammer method. Twelve points were uniformly selected in the circumferential direction of the housing, and three points were uniformly selected along the axial direction of the housing. The test was completed using the single-point response and multi-point excitation methods. The modal parameters were obtained by identifying the modal parameters. According to the analysis of the material properties, the elasticity and shear moduli have a significant influence on the modal parameters. The relationship between their values and modal frequencies was obtained by analyzing the influence of these two parameters on the modal parameters. Finally, the parameter range was determined and a reasonable value was obtained. Combining the experimental and simulation results, the material parameters of each motor component were determined and are listed Tab. 5.

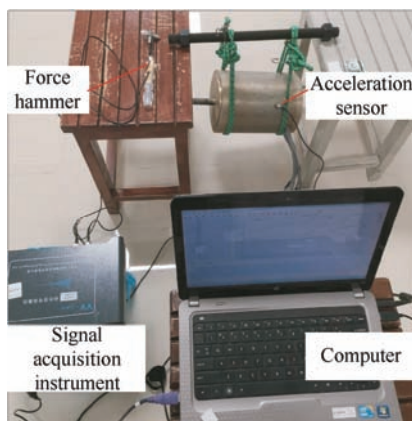



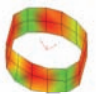

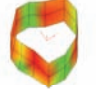
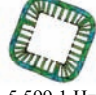

Fig. 20 Modal test of the whole machine

Tab. 5 Material parameters

Parts	Density/(kg/m <sup>3</sup> )	Elasticity modulus/Pa	Poisson's ratio	Shear modulus/Pa
Effective winding	6 550	$E_x=E_y=4.42 \times 10^8$ $E_z=1.3 \times 10^{10}$	0.3	$G_{xy}=7.4 \times 10^7$ $G_{yz}=G_{xz}=2.1 \times 10^9$
Stator	7 700	$E_x=E_y=2.06 \times 10^{11}$ $E_z=1.3 \times 10^{11}$	0.27	$G_{xy}=5.4 \times 10^{10}$ $G_{yz}=G_{xz}=3.3 \times 10^{10}$
Housing and endcaps	2 800	$E_x=E_y=E_z=7.83 \times 10^{10}$	0.33	$G_{xy}=G_{yz}=G_{xz}=2.94 \times 10^{10}$

Tab. 6 lists a comparison of the frequency and mode shapes of the simulation and experiment. The results showed that the simulation error was small and within an acceptable range.

Tab. 6 Simulation and experimental modal results

Order	Simulated	Measured	Error(%)
2	 1 726.5 Hz	 1 732.4 Hz	0.3
3	 3 365.6 Hz	 3 346.7 Hz	0.56
4	 5 599.1 Hz	 5 513.6 Hz	1.5

### 5 Vibration and noise analysis

The basic process of the vibration and noise analysis is shown in Fig. 21. First, the electromagnetic performance is simulated and analyzed. The inner surface of the stator is selected as the electromagnetic force acting on the stator surface. The electromagnetic force is then stretched along the axial direction and its three-dimensional form is obtained. Meanwhile, through modal analysis, we obtained the motor frequency, damping ratio, and modal shape. Subsequently, the electromagnetic force was applied to the motor structure after modal analysis, and the surface vibration acceleration of the housing was calculated. Finally, the envelope surface was established, and the vibration acceleration was used as the excitation source to complete the noise simulation.

The radial force is the most important factor affecting electromagnetic vibration. Radial forces with different orders have different shapes and contributions to the vibration. Through harmonic

response analysis, the influence of each radial force harmonic on vibration was obtained.

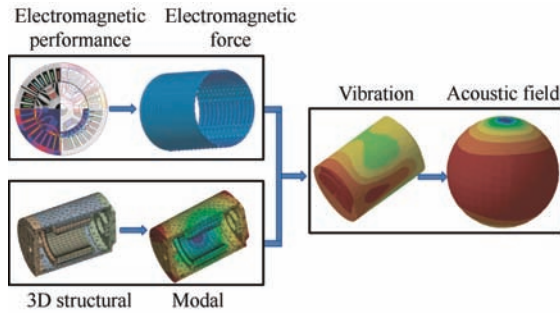


Fig. 21 Basic process of vibration and noise analysis

The mechanical impedance method is commonly used to analyze the vibration of a motor. The parameters of the electrical system were compared to those of the mechanical system to facilitate the understanding of the electrician. The vibrations in the electrical and mechanical systems are described by differential equations<sup>[26-28]</sup>.

If the spatial order of the radial force is greater than two, the acceleration can be expressed as

$$\ddot{Y} \approx \frac{4\pi^2 F_m}{A(r^2 - 1)^2} \cdot \frac{f_\varepsilon^2}{\left(\frac{f_\varepsilon}{f}\right)^2 - 1} \quad (10)$$

where  $F_m$  is the radial force amplitude,  $r$  is the spatial order of the radial force,  $f_\varepsilon$  is the frequency of the radial force,  $f$  is the natural frequency of the motor, and  $A$  is the influence coefficient of the motor size and material on the acceleration.

For the vibration response of the radial force with zero-order and first-order<sup>[29]</sup>, the response is the same as that of other general orders. The difference lies in the expression of the motor stiffness and mass, which can be approximated as

$$\ddot{Y} \approx \frac{4\pi^2 F_m}{B} \cdot \frac{f_\varepsilon^2}{\left(\frac{f_\varepsilon}{f}\right)^2 - 1} \quad (11)$$

where  $B$  is the influence coefficient of the motor size and material on acceleration. The vibration responses caused by the different orders of radial forces are closely related to the motor material parameters. Both  $A$  and  $B$  are the products of the material parameters and corresponding coefficients, which depend on the

order of the radial force. For special orders like the first-order and zero-order, a smaller coefficient needs to be multiplied, so that the value of  $B$  is less than that of  $A$  for the same motor. Therefore, the vibration caused by the zero-order and first-order radial force will be larger than those caused by other radial force harmonics.

Fig. 22 shows the harmonics of the accelerations of the initial and optimized motors at 900 r/min and 2 N · m. It can be observed that the acceleration peaks of the two motors are consistent. The acceleration peaks occurred at 15 Hz ( $f_r$ ), 555 Hz ( $37f_r$ ) and 1 785 Hz ( $119f_r$ ). According to the above radial pressure analysis, there is a UMF at  $f_r$  and  $37f_r$ ; thus, the vibrations are more pronounced at these two frequencies. The acceleration was also large at  $119f_r$ , because it was close to the 2-order natural frequency (1 726.5 Hz). The vibration at this frequency is caused by resonance and not by the electromagnetic force. The acceleration amplitude of the optimized motor has an obvious decreasing trend, and its maximum value decreases from 0.57 m/s<sup>2</sup> to 0.35 m/s<sup>2</sup>, a decrease of 38.6%. The amplitude of the electromagnetic force with high frequency is small, hence it does not cause significant vibration.

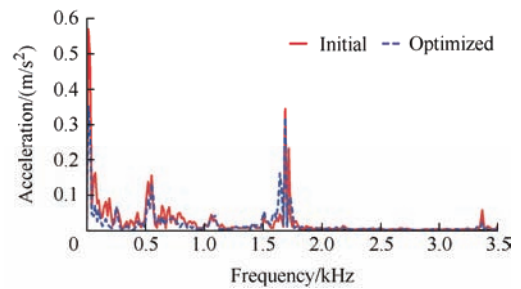


Fig. 22 Acceleration frequency spectrum

The sound pressure  $P_m$  and acceleration  $\ddot{Y}$  are closely related, and the relationship can be expressed as follows

$$P_m = \frac{\rho C \ddot{Y}}{2\pi f} \quad (12)$$

where  $\rho$  is the density of the medium and  $C$  is the speed of sound.

The result of the sound power was unrelated to the measurement distance. This is an objective quantity

that describes the level of noise. Therefore, in this study, sound power was selected as the reference noise level. The sound power level (SWL) can be expressed as

$$L_w = 20 \lg \left( \frac{P_m}{P_0} \right) + 10 \lg 4\pi d^2 \quad (13)$$

where  $P_0$  is the reference sound pressure at  $P_0=2 \times 10^{-5}$  Pa;  $d$  is the distance from the sound source to the test point.

The result of the vibration response was regarded as the excitation; the outer surface of the motor was extracted to form an envelope surface, and the electromagnetic noise was simulated and analyzed.

It can be observed from Fig. 23 that the noise and acceleration peaks are in good agreement. For the two motors, the amplitude of the SWL is large at  $f_r$ ,  $37f_r$  and  $119f_r$ . Because the accelerations at these frequencies are relatively large, they also generate relatively large amounts of noise. The overall trends of the two motors were similar. After optimization, the amplitude of the SWL decreased overall. From the average level, the root-mean-square value of the SWL decreased from 32 dB to 25 dB, and the noise level was significantly.

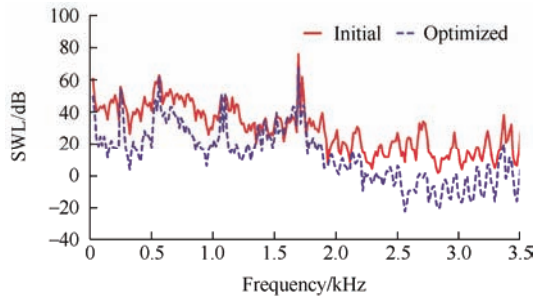


Fig. 23 Sound power level spectrum

## 6 Experimental verification

The accuracy of the FE analysis was verified after the experiments. Fig. 24 shows the test platform. The acceleration sensor was glued to the outer surface of the housing and the microphone was placed approximately 400 mm above the initial prototype. A dSPACE1005 controller was used to control the on-load operation of the prototype. The time-domain signals of acceleration and sound pressure were collected by the signal acquisition instrument, and then the spectrum of the time-domain signals was analyzed.

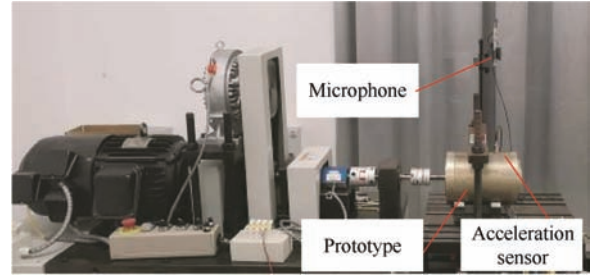


Fig. 24 Experimental platform

Fig. 25a compares the experimental and simulated results of the acceleration at 900 r/min and 2 N · m. The fundamental frequency of the acceleration is 15 Hz. The maximum amplitude of acceleration is at the fundamental frequency. In addition,  $37f_r$  and the 2-order natural frequency also have larger vibrations. At these frequencies, the experimental results and simulation results have larger values. Because the simulation model is reasonably simplified and the influence of mechanical vibration cannot be eliminated during the experiment, the simulation results are slightly different from the experiment. However, the simulation can well reflect the vibration peaks of the experimental results, so the simulation results are credible.

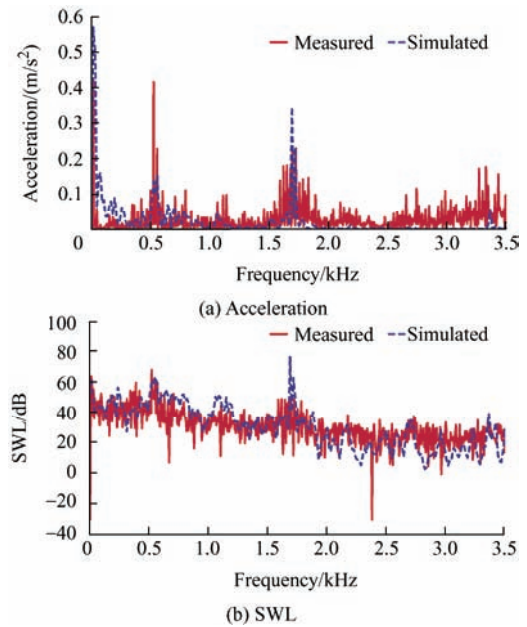


Fig. 25 Experiment and simulation comparison

The measured sound pressure was converted into SWL. Fig. 25b shows a comparison of the experimental and simulated SWL results. The results show that the main peaks are at  $f_r$ ,  $37f_r$  and the 2-order natural frequency. The trend of the simulation results was similar to that of the experimental results.

Because platform noise cannot be eliminated and instrument noise cannot be avoided, the simulation results differ slightly from the experimental results.

## 7 Conclusions

In this study, the vibration and noise of a new asymmetric modular PMaSynRM were analyzed in detail, and an optimized structure was proposed. Through the prototype experiment, the rationality and effectiveness of the analysis were verified, and the following conclusions were drawn.

(1) The frequency and order of the radial pressures obtained from the simulation were consistent with the analytical analysis. The vibration and noise of the PMaSynRM were closely related to the radial pressures. In the asymmetric motor, the UMF intensified the vibration. The radial pressures were generated by the interaction of two different flux densities. The permeability of the rotor affects the flux density. Therefore, the corresponding radial pressure can be reduced by reducing the amplitude of the rotor permeance harmonics.

(2) After the optimization, the acceleration and SWL of the motor decreased significantly. The maximum acceleration decreased from  $0.57 \text{ m/s}^2$  to  $0.35 \text{ m/s}^2$ , a decrease of 38.6%. The root mean square value of the SWL decreased from 32 dB to 25 dB, a decrease of 21.9%. The optimized motor significantly improved the vibration and noise performance. The validity of the simulation results was experimentally verified.

## References

- [1] H Cai, B Guan, L Xu, et al. Low-cost ferrite PM-assisted synchronous reluctance machine for electric vehicle. *IEEE Trans. Ind. Electron.*, 2014, 61(10): 5741-5748.
- [2] M Z Islam, A Arafat, S S R Bonthu, et al. Design of a robust five-phase ferrite-assisted synchronous reluctance motor with low demagnetization and mechanical deformation. *IEEE Trans. Energy Convers.*, 2019, 34(2): 722-730.
- [3] B Ma, S Yu, F Zhang, et al. Structure and cooling system design of new dual stator permanent magnet assisted reluctance motor. *Journal of Electrical Engineering*, 2020, 15(1): 55-61.
- [4] M Xu, G Liu, Q Chen, et al. Design and optimization of a fault tolerant modular PMaSynRM with torque ripple minimization. *IEEE Trans. Ind. Electron.*, 2021, 68(9): 8519-8530.
- [5] H Lan, J Zou, Y Xu, et al. Investigation of unbalanced magnetic force in permanent magnet synchronous machines with asymmetric design. *IEEE Trans. Magn.*, 2018, 54(11): 8203305.
- [6] J Li, H Mahmoud, M Degano, et al. Vibration analysis of permanent-magnet-assisted synchronous reluctance machines. *IEEE Int. Conf. Electr. Mac. Syst.*, 11-14 August, 2019, Harbin, China. IEEE, 2019: 1-6.
- [7] S Abdi, E Abdi, H Toshani, et al. Vibration analysis of brushless doubly fed machines in the presence of rotor eccentricity. *IEEE Trans. Energy Convers.*, 2020, 35(3): 1372-1380.
- [8] Z Q Zhu, M L M Jamil, L J Wu, et al. Influence of slot and pole number combinations on unbalanced magnetic force in PM machines diametrically asymmetric windings. *IEEE Trans. Ind. Appl.*, 2013, 49(1): 19-30.
- [9] F Rezaee-Alam, B Rezaeealam, J Faiz, et al. Unbalanced magnetic force analysis in eccentric surface permanent-magnet motors using an improved conformal mapping method. *IEEE Trans. Energy Convers.*, 2017, 32(1): 146-154.
- [10] C Lin, S Wang, M Moallem, et al. Analysis of vibration in permanent magnet synchronous machines due to variable speed drives. *IEEE Trans. Energy Convers.*, 2017, 32(2): 582-590.
- [11] W Deng, S Zuo. Electromagnetic vibration and noise of the permanent-magnet synchronous motors for electric vehicles: An overview. *IEEE Trans. Transport. Electric.*, 2019, 5(1): 59-70.
- [12] Y Mao, G Liu, W Zhao, et al. Vibration prediction in fault-tolerant flux-switching permanent-magnet machine under healthy and faulty conditions. *IET Electric Power Applications.*, 2016, 11(1): 19-28.
- [13] Y Lu, J Li, R Qu, et al. Electromagnetic force and vibration analysis of permanent magnet assisted synchronous reluctance machines. *IEEE Trans. Ind. Appl.*, 2018, 54(5): 4246-4256.
- [14] Z Song, C Liu, H Zhao. Investigation on magnetic force of a flux-modulated double-rotor permanent magnet synchronous machine for hybrid electric vehicle. *IEEE Trans. Transport. Electric.*, 2019, 5(4): 1383-1394.
- [15] Z Tang, P Pillay, A M Omekanda, et al. Young's modulus for laminated machine structures with particular reference

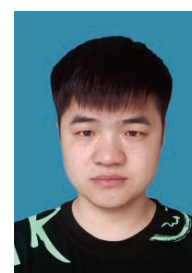


- to switched reluctance motor vibrations. *IEEE Trans. Ind. Appl.*, 2004, 40(3): 748-754.
- [16] S Hu, S Zuo, H Wu, et al. An analytical method for calculating the natural frequencies of a motor considering orthotropic material parameters. *IEEE Trans. Ind. Electron.*, 2019, 66(10): 7520-7528.
- [17] F Chai, Y Li, Y Pei, et al. Accurate modelling and modal analysis of stator system in permanent magnet synchronous motor with concentrated winding for vibration prediction. *IET Electric Power Applications.*, 2018, 12(8): 1225-1232.
- [18] X Wang, X Sun, P Gao, et al. Study on the effects of rotor-step skewing on the vibration and noise of a PMSM for electric vehicles. *IET Electric Power Applications.*, 2019, 14(1): 131-138.
- [19] J Boisson, F Louf, J Ojeda, et al. Analytical approach for mechanical resonance frequencies of high-speed machines. *IEEE Trans. Ind. Electron.*, 2014, 61(6): 3081-3088.
- [20] Y Mao, G Liu, W Zhao, et al. Low-noise design of fault-tolerant flux-switching permanent-magnet machines. *IET Electric Power Applications.*, 2018, 12(6): 747-756.
- [21] S Wang, J Hong, Y Sun, et al. Filling force valley with interpoles for pole-frequency vibration reduction in surface-mounted PM synchronous machines. *IEEE Trans. Ind. Electron.*, 2020, 67(8): 6709-6720.
- [22] H Yang, Y Lim, H Kim, et al. Acoustic noise/vibration reduction of a single-phase SRM using skewed stator and rotor. *IEEE Trans. Ind. Electron.*, 2013, 60(10): 4292-4300.
- [23] W Zhang, Y Xu, Y Huang, et al. Reduction of high-frequency vibration noise for dual-branch three-phase permanent magnet synchronous motors. *Chinese Journal of Electrical Engineering.*, 2020, 6(2): 42-51.
- [24] G Xu, Z Jia, W Zhao, et al. Multi-objective optimization design of inset-surface permanent magnet machine considering deterministic and robust performances. *Chinese Journal of Electrical Engineering.*, 2021, 7(3): 73-87.
- [25] Y Mao, W Zhao, S Zhu, et al. Vibration investigation of spoke-type PM machine with asymmetric rotor considering modulation effect of stator teeth. *IEEE Trans. Ind. Electron.*, 2021, 68(10): 9092-9103.
- [26] K H Yim, J W Jang, G H Jang, et al. Forced vibration analysis of an IPM motor for electrical vehicles due to magnetic force. *IEEE Trans. Magn.*, 2012, 48(11): 2981-2984.
- [27] A K Putri, S Rick, D Franck, et al. Application of sinusoidal field pole in a permanent-magnet synchronous machine to improve the NVH behavior considering the MTPA and MTPV operation area. *IEEE Trans. Ind. Appl.*, 2016, 52(3): 2280-2288.
- [28] S Das, O Gundogmus, Y Sozer, et al. Wide speed range noise and vibration mitigation in switched reluctance machines with stator pole bridges. *IEEE Trans. Power Electron.*, 2021, 36(8): 9300-9311.
- [29] S Wang, J Hong, Y Sun, et al. Analysis of zeroth mode slot frequency vibration of integer slot permanent magnet synchronous motors. *IEEE Trans. Ind. Electron.*, 2020, 67(4): 2954-2964.



**Guohai Liu** (M'07-SM'15) received the B.Sc. degree from Jiangsu University, Zhenjiang, China, in 1985, and the M.Sc. and Ph.D. degrees from Southeast University, Nanjing, China, in 1988 and 2002, respectively, in Electrical Engineering and Control Engineering.

He has been with Jiangsu University since 1988, where he is currently a Professor in the School of Electrical and Information Engineering. From 2003 to 2004, he was a Visiting Professor with the Department of Electronic and Electrical Engineering, The University of Sheffield, Sheffield, UK. His teaching and research interests include electrical machines, motor drives for electric vehicles and intelligent control. He has authored or co-authored over 200 technical papers and 4 textbooks, and holds 30 patents in these areas.



**Akang Gao** received his B.Sc. degree in Electrical Engineering from Jiangsu University, Zhenjiang, China, in 2019. And he is currently working toward the M.Sc. degree in Electrical Engineering, Jiangsu University, Zhenjiang, China.

His research interests include the optimization design and vibration noise simulation of permanent-magnet machines.



**Qian Chen** (M'16-SM'20) received the B.Sc. and Ph.D. degrees from Jiangsu University, Zhenjiang, China, in 2009 and 2015, respectively, in Electrical Engineering and Control Engineering.

He has been with Jiangsu University since 2015, where he is currently a Professor in the School of Electrical and Information Engineering. His current research interests include electric machine design, modeling, fault analysis, and intelligent control.



**Yanxin Mao** received the M.Sc. degree from Wuhan Institute Physics and Mathematics, Chinese Academy of Sciences, China, in 2004, and the Ph.D. degree from Jiangsu University, China, in 2018.

Since 2004, she has been with the School of Electrical and Information Engineering, Jiangsu University, where she is currently an Associate Professor. Her research interest is vibration and acoustic noise of permanent magnet machines.



**Gaohong Xu** received B.Sc., M.Sc., and Ph.D. degrees from Jiangsu University, Zhenjiang, China, in 2009, 2011 and 2018, respectively, in Electrical Engineering.

She has been with Jiangsu University since 2018, where she is currently a Lecturer in School of Electrical and Information Engineering. Her current research interests include computation of electromagnetic fields for permanent-magnet machine and electric

machine design.